Detached Eddy Simulation of Supersonic Combustion Development in a Confined Environment: a Comparative Study for two Equivalence Ratios

Guillaume Pelletier[1], Marc Ferrier[2], Axel Vincent-Randonnier[3], Arnaud Mura[4]

Abstract

Reactive Delayed Detached Eddy Simulations (DDES) of hydrogen injected into a transverse supersonic flow of vitiated air are conducted in a confined environment. The corresponding experimental conditions are studied in the LAPCAT-II combustor operated in the LAERTE facility of ONERA Palaiseau Research Center. Due to thermal coating, the wall surfaces of this combustor feature a significant wall roughness, the mean characteristic height of which is 65 µm. The effects of this wall roughness on the turbulent reactive flow development is taken into account within the sand-grain modeling framework.
Experimental results exhibit two distinct combustion modes depending on the global feeding equivalence ratio: one is characteristic of supersonic combustion and the other one is characteristic of partially thermally choked flow. Numerical simulations can reproduce these behaviors provided that wall roughness is taken into account.

Keywords: *scramjet, combustion, DES*

Nomenclature

Latin

C_{DES} − a constant for the (D)DES method

f_{DDES} − RANS / LES transition function for DDES

F_1 − k-ϵ / k-ω transition function for k-ω SST turbulence model

$h^{\circ}_{f,\alpha}$ − enthalpy of formation of species α

k − turbulence kinetic energy

l − turbulence length scale

P − pressure

T − temperature

u − flow velocity in the x-direction

q − mass flow of vitiated air

S_{ξ} − segregation rate

$\tilde{V}$ − variance or standard deviation

y − distance from the wall

Yα − mass fraction of species α

Greek

β* − a constant for the k-ω SST turbulence model

Δ − cell size

ϵ − turbulence dissipation rate

v − kinematic viscosity

Φ − equivalence ratio

ω − turbulence specific dissipation rate

Ω_{α} − production rate of species α

Ω_T − heat release rate

ξ − mixture fraction

Superscripts

+ − relative to wall variables

Subscripts

t − relative to stagnation or total conditions

j − relative to injection conditions

1. Introduction

Non-premixed supersonic combustion has been extensively studied over the last thirty years, and a huge amount of well-documented experimental databases have been documented in the literature [1, 2, 3,

---

[1]*ONERA, Université Paris Saclay, F-91123 Palaiseau, France, guillaume.pelletier@onera.fr*

[2]*ONERA, Université Paris Saclay, F-91123 Palaiseau, France, marc.ferrier@onera.fr*

[3]*ONERA, Université Paris Saclay, F-91123 Palaiseau, France, axel.vincent@onera.fr*

[4]*Ecole Nationale Supérieure de Mécanique et d Aérotechnique, Pprime Institute UPR3346 CNRS, Futuroscope, France, 86961, arnaud.mura@isae-ensma.fr*

4, 5].The LAPCAT-II experiments conducted in the LAERTE facility of ONERA Palaiseau Research Center [6, 7] gather such data within a scramjet-like environment with conditions representative of a Mach 6 supersonic flight.

Unlike supersonic combustion experiments conducted in open geometries, such as the one carried out by Gamba *et al.* [8], results obtained in confined environment can exhibit different combustion stabilization mechanisms depending on the global equivalence ratio, from a totally started engine to a completely thermally choked flow. In particular, in the LACAT-II experiments, two combustion modes have been highlighted, one corresponding to a supersonic mode, and the other one, to a partially choked mode [7].

Computational investigation of such reactive flows is challenging for many facets of the corresponding models including the numerical scheme accuracy, the physical models of turbulence, combustion turbulence chemistry interaction or the wall modeling. The issue of turbulent mixing representation may be addressed through several options. The RANS framework remains rather questionnable since wall-bounded compressible turbulent flows exhibit a strong dependency to some compressible patterns which are intrinsically unsteady, e.g., shock boundary layers interactions. A more relevant framework, able to give a more satisfactory representation of turbulent mixing may lie in the LES. The detailed computation of the wall dynamics and heat transfer may have little effect on the bulk flow development in strongly separated flow, and this allows low-resolved LES to be performed at the wall. This is in contrast to flows that display complex interactions between shock waves and boundary layers, or when the target is to study wall fluxes, which require the boundary layers to be well represented. Such an objective can be reached with a LES meshing of the boundary layer, this option remains however very expensive for internal aerodynamics such as the one involved in a combustion chamber. In this context, the simulations results achieved by Fureby *et al.* [9] on the LAPCAT-II geometry are quite remarkable. The other possibility, which is retained in the present study, is to combine the LES with a cheaper approach close to the walls. This is the aim of the DES approach combining RANS modeling of the boundary layer with LES models in the far region.

Furthermore, previous studies of the LAPCAT-II combustor [7, 10] pointed out that wall roughness needed to be taken into account. In these studies, the wall roughness influence on the skin friction was mimicked by and arbitrary increase of the molecular viscosity coefficient while the present work is concerned with a more general methodology.

The manuscript is organized as follows: the experimental setup and main test results are presented in section 2. Then, a description of the computational model is provided in section 3, including a brief presentation of the roughness model. The analysis of the computational results in section 4 includes a comparison of the numerical simulation results with experimental data followed by a comparative study of combustion stabilization mechanisms for both combustion modes.
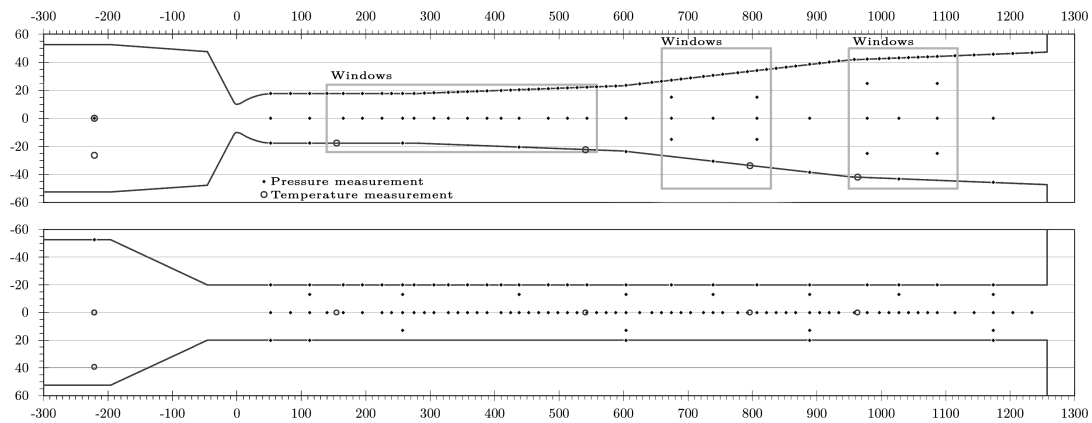
2. Experimental set-up

The LAPCAT-II combustor (see Figure 1) is a constant width combustor composed of four successive sections. The first one, which operates as an isolator, has a constant height of 35.4 mm and spans over 215 mm. This isolator is followed by three diverging sections characterized by a one-degree (318 mm length), a three degree (354.5 mm length), and a one degree (305 mm length) diverging half angle preventing the high-speed flow from thermal chocking.

This combustion chamber is fed with a hot vitiated airstream, which is generated by the preliminary combustion of a H_2-air mixture followed by O_2 replenishment to keep the value of the oxygen molar fraction equal to 0.21. This combustor is fueled with hydrogen injected through two sonic injectors (2 mm diameter) located at x = 200 mm in the symmetry plane of the top and bottom walls of the test section. It is equipped with pressure sensors along the walls and features large optical accesses allowing OH^* and Schlieren visualizations.

The combustion chamber is made of a copper alloy and its inner walls are coated with a 300 μm thick

Thermal Barrier Coating (TBC) made of Yttria-stabilized Zirconia (Yttria denotes Yttrium oxide). This TBC surface is similar to sandpaper and it has been characterized using Scanning Electron Microscopy (SEM), showing an average characteristic roughness size of around 65 μm, see Figure 2.

Fig 1. Geometry of the LAPCAT-II combustor.
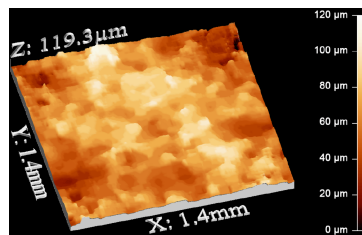
**Fig 2.** SEM 3D reconstruction of the LAPCAT-II surface.

The present study is focused on the consideration of two experimental runs: 20151123-R10 and 20151123-R09, hereafter denoted as cases A and B, the conditions of which are gathered in Table 1, where the six first columns gather conditions relative to the vitiated air and the three last ones, relative to the injection. The main difference between these two cases is the equivalence ratio.

Table 1. Experimental conditions

Ref.	P_t (bar)	T_t (K)	Y_{N_2}	Y_{O_2}	Y_{H_2O}	q (g/s)	$P_{t,j}$ (bar)	$T_{t,j}$ (K)	Φ
case A	4.03	1704	0.5775	0.2554	0.1671	290.1	3.91	305	0.121
case B	4.07	1706	0.5852	0.2476	0.1672	291.7	4.78	300	0.145

Figure 3 displays OH* chemiluminescence superimposed on Schlieren imaging for cases A (left) and B (right). It seems worth recalling that the injection is located at x = 200 mm. As emphasized in reference [7], this injection is responsible for the shock reflections that can be observed in grayscale in Figure 3, particularly for case A. For this case, the OH* emission, represented in red-scale, shows that the combustion starts far downstream of the H_2-injection at abscissas that are larger than 260 mm for the upper wall and larger than 300 mm for the lower wall. In these experimental conditions, the upper and lower combustion stabilization zones are not established at the same location and moves back and forth on the top and bottom walls. The flow-field does not seem to be dramatically distorted by the combustion development. This indicates that this is a rather standard mode of supersonic combustion where the injected fuel mixes with the vitiated air-stream and, after a certain induction time, thermal runaway takes place leading to OH* production.

This is in sharp contrast with case B for which the flow exhibits large boundary layer separations, between 250 and 280 mm, that lead to the formation of a strong shock waves system. As indicated by the OH* emission, combustion takes place mainly in these separation zones so that the following scenario is proposed for this combustion stabilization process: as the equivalence ratio is increased, the increase in the heat release rate leads the flow to approach thermal choking giving rise to boundary layer separation. These separation zones feature regions of low velocity and high temperatures that act as flame holders for the combustion.
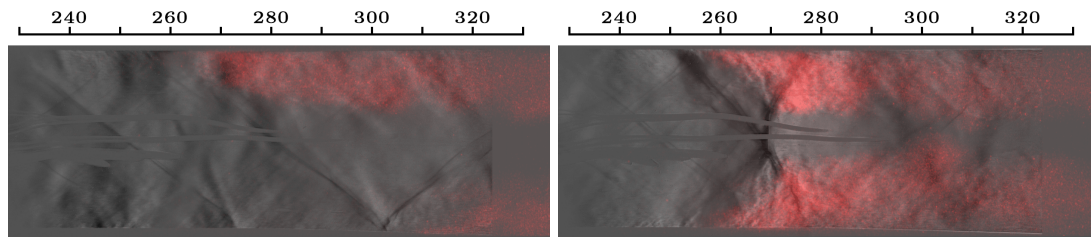
**Fig 3.** Strioscopy (gray-scale) and OH* chemiluminescence (red-scale) for case A (left) and case B (right).

3. Description of the computational model

The present study is conducted with the ONERA computational fluid dynamics code CEDRE [11] which is a multi-physics platform relying on specific solvers to handle complex flow simulations. This study makes use of the finite volume three-dimensional compressible and reactive Navier-Stockes solver CHARME.

3.1. Computational setup

The computational domain spans from 195 mm before the throat of the Mach 2 De Laval nozzle up to 650 mm downstream. This domain covers only the started part of the combustor. In order to reduce the computational cost of the simulations presented in this study only half of the combustion chamber is considered and it should be precised that only the averaged results will be considered in the next parts of the analysis. The boundary conditions are delineated in Figure 4.

- Green boundaries correspond to inlet conditions. The vitiated air inlet, on the left side of the figure, is specified with stagnation pressure and temperature. The velocity is adjusted so as to enforce the mass flow rates, which are determined from a chocked nozzle condition. The hydrogen injection is modeled as a surface where sonic inlet Dirichlet conditions are applied.

- Blue boundaries correspond to no-slip boundary conditions, the roughness model is applied to these walls.

- Red boundaries represent the symmetry plane.

- Yellow boundaries on the right side represent a supersonic outlet where all quantities are determined from extrapolation rules.
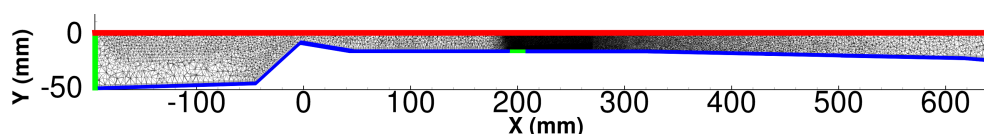

Fig 4. Computational domain retained to perform the numerical simulation of the LAPCAT-II combustion chamber. Boundary conditions are delineated in color.

3.2. Computational mesh

The mesh is composed of prism layers along the walls and tetrahedrons in the rest of the computational domain. It features approximately 23.4 millions of cells. The fuel injection and mixing layer regions are refined to obtain a satisfactory description of the mixing layer growth rate. The characteristic cell size in the mixing layer region is computed using a criterion $\Delta = \Delta v_x / \left[10 \max\left(\partial v_x / \partial y\right)\right]$ which is here expressed considering a 2D mixing layer. The quantity Δv_x represents the velocity difference between the two layers and $\partial v_x / \partial y$ the velocity gradient along the transverse direction. A first RANS computation is conducted so as to locate high vorticity zones in the wake of the injection. The computed norm of the vorticity field is subsequently used as a threshold to apply the above criterion. Figure 5 gives a view of the mesh in the vicinity of the injection and of the associated mixing layer. The profile of the dimensionless height y^+ obtained in the plane Z = 0 for the computational cells at the wall location shows that, in the region of interest, the values of y^+ remains smaller than unity.
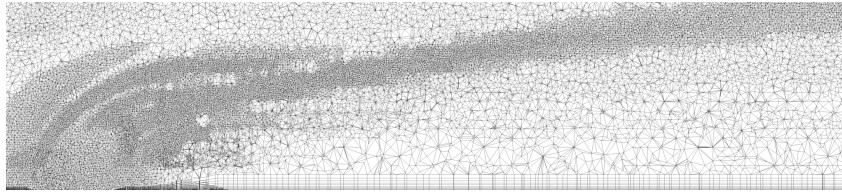
Fig 5. Mesh in the vicinity of the injector and mixing layer.
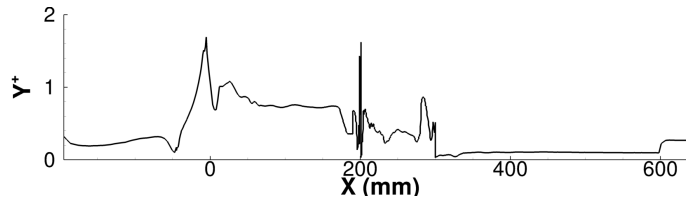
Fig 6. Profile of y^+ in the symmetry plane.

In the following, the computational results are mirrored with respect to the symmetry plane, in order to make easier the comparison with experimental visualizations.

3.2.1. Delayed Detached Eddy Simulation

In this study, Hybrid RANS / LES model is not only used to coarsen mesh near the walls (and then to reduce computation time), but also to take into account wall roughness through a model that is developed within the RANS framework (see section 3.2.2). The hybridization used here enters the Delayed Detached Eddy Simulation (DDES) framework [12]. Following Strelets'work [13], this framework is here applied to Menter's k-ω SST turbulence model [14]. In the DDES turbulence modeling approach, the RANS turbulence length scale l_{RANS} is replaced by l_{DDES} in such manner that:

$$l_{DDES} = l_{RANS} - f_{DDES} \times \max(0, l_{RANS} - C_{DES}\Delta) \qquad (1)$$

In Eq.1, the Fan *et al.* [15] formulation is retained for f_{DDES}:

$$f_{DDES} = 1 - \tanh\left(\frac{1}{\omega}\max\left(\frac{500\nu}{y_w}, \frac{\sqrt{k}}{\beta^* y_w}\right)\right) \qquad (2)$$

As most of the constants involved in the Menter's k-ω SST model, the value of C_{DES} is blended using the F_1 transition function, which is equal to unity in the near wall region and going to zero far from the walls:

$$C_{DES} = (1 - F_1)C_{DES}^{k-\epsilon} + F_1 C_{DES}^{k-\omega} \qquad (3)$$

Both constants values $C_{DES}^{k-\epsilon}$ and $C_{DES}^{k-\omega}$ have been calibrated to 0.61 and 0.78, respectively.

3.2.2. Roughness Model

The equivalent sand grain approach is retained in the present study to take wall roughness into account. The objective of this methodology is to reproduce the skin friction increase induced by wall roughness. This skin friction increase can be related to a downward shift of the velocity profile within the logarithmic region of the boundary layer [16, 17]. Correlations evaluating this velocity shift as a function of a quantity suited to represent the roughness, i.e., the equivalent sand grain height k_s, have been proposed in the literature [16, 17, 18, 19]. Within the RANS framework, a common solution consists in modifying the wall boundary conditions of the turbulence models so as to reproduce the skin friction increase, or equivalently, the velocity shift [20, 21, 22, 23, 24]. In the present study, the methodology developped by Aupoix et al. [20] is retained and Grigson's correlation [19] is used to evaluate the velocity shift.

This methodology has been assessed by comparison with supersonic velocity profiles measured over a rough flat plate for roughness of different types and k_s [25]. Two- and Three-dimensional uniformly spaced roughness elements have been used as well as three sand-grain roughened plates corresponding to 20, 36 and 82 grit sandpaper. The Mach number out of the boundary layer was around 2.7 and the unit Reynolds number around 1.2×10^7. Results of this comparison are presented on Fig.7. The agreement with the experiment is quite satisfactory.
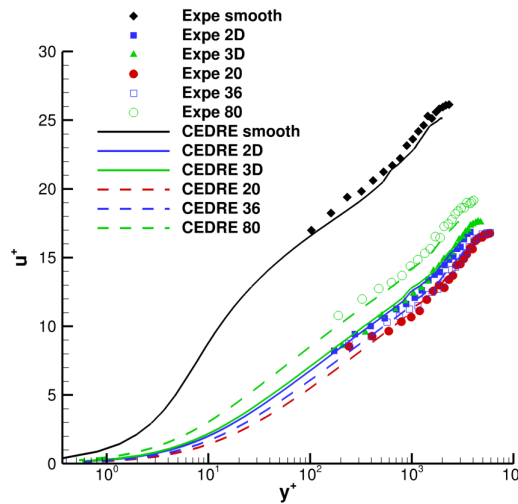
Fig 7. Supersonic velocity profiles on rough walls: simulation versus experiment.

3.2.3. Chemical production rates

The averaged chemical production rates $\bar{\Omega}_\alpha$ that appear in the species mass fraction transport equations are modeled within the Well-Stirred Reactor (WSR) or quasi-laminar framework, which neglects the possible influence of unresolved fluctuations of composition at the resolved level, i.e, $\bar{\Omega}_\alpha = \Omega_\alpha\left(\widetilde{T}, \widetilde{Y}_\alpha\right)$. It is recalled that, in the present study, combustion is expected to be chemistry-controlled, at least for case A (this point is discussed in more details in section 4). The corresponding reactions rates are evaluated from the detailed chemical scheme of Jachimowski [26].

3.3. Numerical Schemes

The numerical treatment of inviscid fluxes makes use of the HLLC (Harten-Lax-van Leer Contact) approximate Riemann solver [27]. Second-order accuracy is achieved via variable extrapolation monotonic using upwind scheme for conservation laws (MUSCL) applied in conjunction with Van Leer flux limiters to ensure monotonicity [28, 29]. The viscous fluxes are evaluated with a second-order centered scheme.
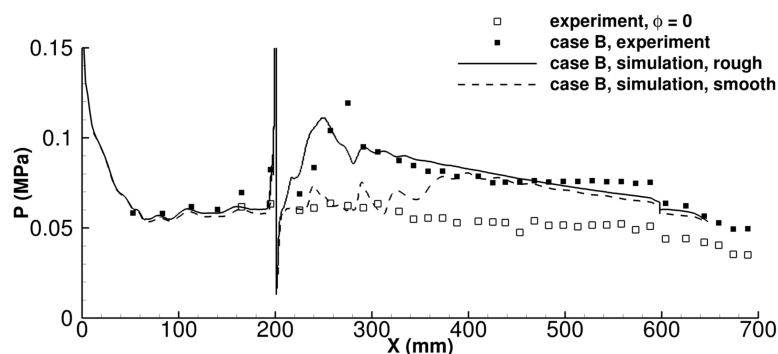
4. Numerical results

In the two next sections, the numerical results are analyzed for cases A and B, and for the smooth and rough wall cases. Numerical simulations are conducted with a time step of 10^{-8}s during approximately 10 ms, which represents 25 residence times in the combustor. The following results are time averaged over the last 6 ms (15 residence times). In order to favor the direct comparison with experimental visualizations, the numerical fields are mirrored according to the XZ plane of symmetry (see Fig.4).

4.1. Comparison to experimental results

Numerical results are compared to experiments in terms of pressure distributions on the top wall in the plane of symmetry on Fig.8 and 9. They are also compared in terms of OH^* and Schlieren visualizations (Fig. 10 and 11). To that end, the computed x-density gradients and the heat release rates are integrated through the numerical domain (according the Z axis). The heat release rates are here computed as $\Omega_T = -\sum_\alpha h^\circ_{f,\alpha}\Omega_\alpha$, where $h^\circ_{f,\alpha}$ is the enthalpy of formation of the species α, and Ω_α, its production rate. It is assumed that this quantity is representative of the OH^* emission field.
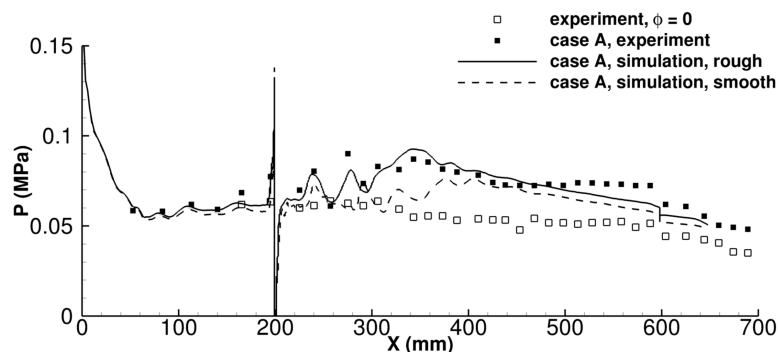
**Fig 8.** Experimental and numerical pressure profiles for rough and smooth walls (case A).


Fig 9. idem FiG.8 (case B).

For both cases, numerical results are significantly improved when wall roughness is considered. For the self-ignition case (A), fuel ignites slightly upstream and combustion is more intense in the rough case

(see Fig.10). This leads to a higher pressure level in the combustor which results in a better agreement with experimental pressure distribution.

For case B, a dramatic change in the flow topology is observed when roughness is taken into account (see Fig.11). Whereas, if smooth walls are considered, the flow topology remains similar to the self-ignition case, the consideration of the roughness model in the simulations allows to reproduce the partially choked flow structure observed in experiment. In particular, the crux-like shock pattern is well captured even if it is located slightly upstream of its experimental position. The combustion stabilization is also clearly intertwined with this particular flow topology. In terms of pressure distribution, the occurrence of this shock pattern, linked to the high heat release rate and to flow separation, is responsible for the pressure peak observed in both experimental and numerical results (see Fig.9).
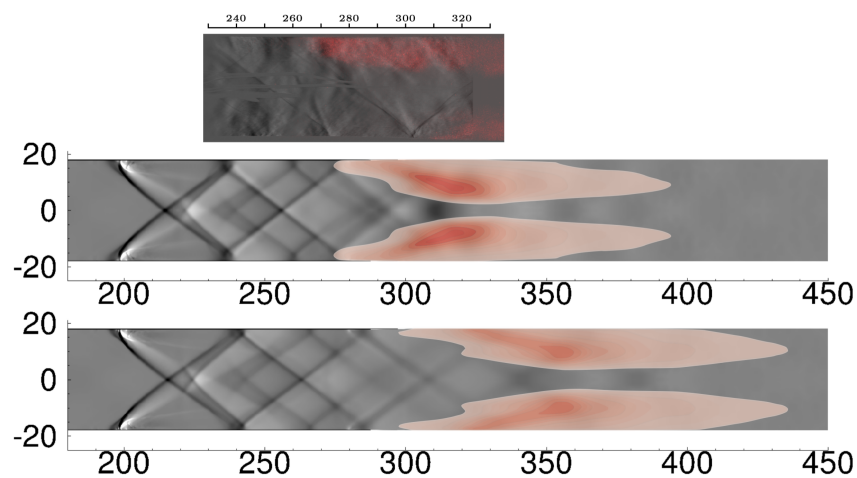
Fig 10. Comparison between simulations and experiments: strioscopy (gray-scale) and OH* chemiluminescence (red-scale) (case A).
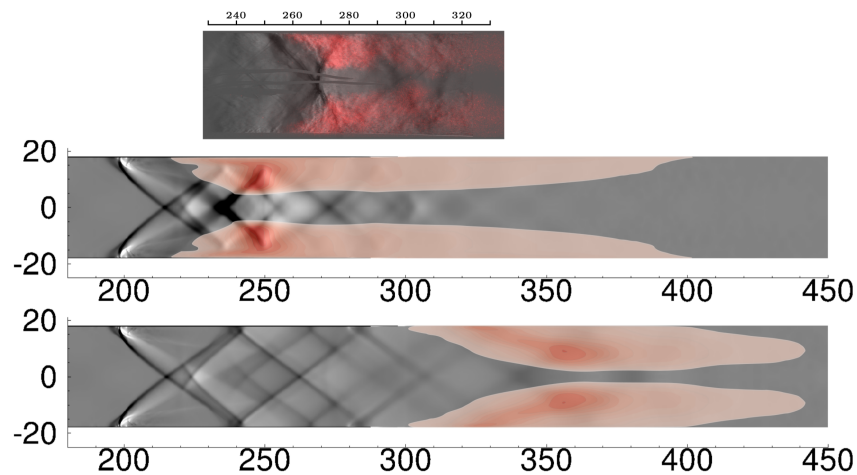

Fig 11. idem Fig.10 (case B).

4.2. Combustion comparative analysis for both combustion modes

Combustion development is now analyzed for both cases, in Fig.12 (case A) and 13 (case B), in terms of heat release rates (Ω_T), segregation rates (S_ξ), HO$_2$ mass fraction (Y_{HO2}) and flow velocity (u_x), in the XY plane of symmetry of the combustor.

The segregation rate is the normalized standard deviation, or variance, of the mixture fraction ξ: $S_\xi = \tilde{V}_\xi/(\tilde{\xi}(1-\tilde{\xi}))$ ($\tilde{V}_\xi = \widetilde{\xi^2} - \tilde{\xi}^2$ is the variance of ξ). The mixture fraction is evaluated by considering the mass fraction of a passive scalar that is injected with the fuel (it is the fuel inlet tracer). The variance of ξ is here calculated by considering the equilibrium between production and dissipation in a transport equation for this quantity. Several expressions for the transport equation for $\tilde{V}_\xi$ can be found in [30]. This equilibrium leads to $\tilde{V}_\xi = c_\xi^{-1}\Delta^2 \frac{\partial \tilde{\xi}}{\partial x_i}\frac{\partial \tilde{\xi}}{\partial x_i}$ with c_ξ^{-1} taken equal to unity. The quantity S_ξ can be used to reference the degree of unmixedness between the reactants at the unresolved scale.
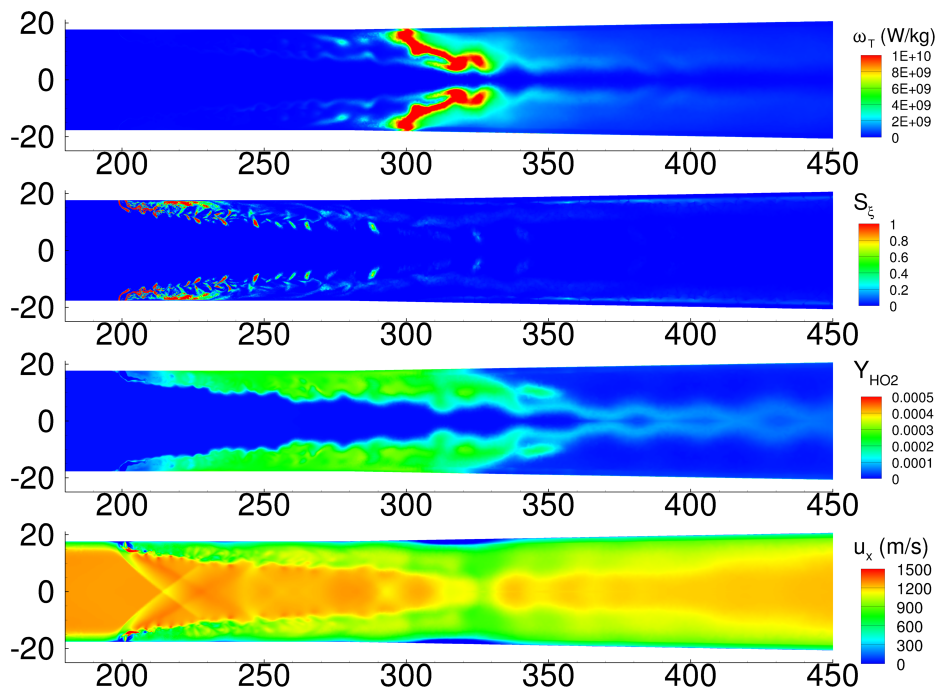
Fig 12. From top to bottom: heat release rate (Ω_T), segregation rate (S_ξ), HO$_2$ mass fraction (Y_{HO2} and longitudinal velocity (u_x) (case A).

For case A, combustion starts at abscissa x = 300 mm, far downstream the fuel injection (x = 200 mm). Over the corresponding distance, fuel mixes up with air, as it is shown by the decay of the segregation rate, and HO$_2$ is produced. This shows that the interval 200 < x < 300 mm can be considered as an induction distance before thermal runaway [31], which characterizes self-ignition. Another evidence of this mode of combustion stabilization is the very large values of the velocity at the location of high heat release rates which precludes the stabilization by flame propagation mechanisms. From these observations, it can be concluded that the WSR approach is relevant for calculating the chemical production rates. In particular, the segregation rates in the combustion zones are very weak, which ensure that the unresolved fluctuations of composition remain negligible.

For case B, the distance between the fuel injection and the combustion stabilization location is significantly smaller. The spatial discrimination between regions of high heat release and regions of high HO$_2$ concentration is less visible compared to case A. At the locations where combustion occurs, large regions of low velocity flow, which are relevant to separated flows, can be observed at the bottom of Fig.13. These velocity values become compatible with a combustion stabilization based on flame propagation. Also, the segregation rates in the combustion zones display locally large values. Therefore, the WSR approach can become unsuited for this case which would certainly benefit from the use of a turbulent combustion model taking into account non-premixed flames characteristics.
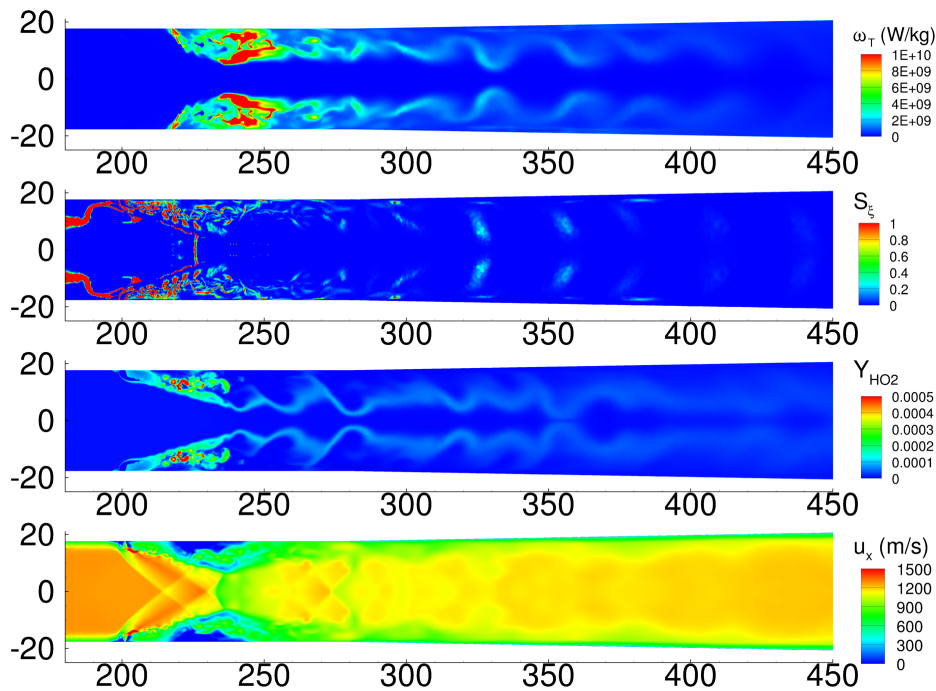
Fig 13. idem Fig.12 (case B).

5. Conclusion

The present study has been focused on the DDES simulations of the LAPCAT-II dual mode ramjet/scramjet combustor. The non-negligible wall roughness induced by the thermal barrier coating deposited on the metallic surface of the combustor is considered. The experimental data exhibit two distinct combustion modes depending on the global equivalence ratio value. The first one, which corresponds to a moderate equivalence ratio, is characteristic of supersonic combustion with self-ignition processes following an induction distance. As the equivalence ratio value is slightly increased, the flow topology changes dramatically. In this second mode, combustion is intertwined with large boundary layer separations and strong shock waves, which are specific of flow near thermal choking conditions.

In the simulations, the wall roughness is taken into account using a sand grain modeling approach. The use of this model significantly improves numerical results: combustion is promoted and experimental trends are recovered. In particular, if wall roughness is not taken into account for the partially choked case, results are similar to the self-ignition case. It is yet not clear how roughness can influence combustion in these experiments. A possible explanation is that the increase of the boundary layer thickness on a rough surface (compared to a smooth one) reduces the apparent cross section of the combustor; the global velocity of the supersonic flow is then smaller and its temperature higher which can promote self-ignition and thermal choking. A second explanation is that the higher near wall turbulent viscosity induced by the roughness model can diffuse into the core flow and then enhance temperature and chemical species transport.

Concerning the combustion modeling, the production rates of chemical species are computed using the Well-Stirred Reactor (WSR) framework. This approach assumes that unresolved compositions fluctuations remain negligible. The level of composition fluctuations can be measured using the segregation rate S_ξ, which provides an estimate of the mixture fraction variance. For the self-ignition case, the levels of segregation rate remain rather weak and then the WSR approach seems to be relevant. For the partially choked case, the proximity between the injection and the combustion zones is associated with large values of S_ξ which may invalidate this combustion model. For future simulations, it would be interesting to include the segregation rate into the turbulent combustion model.

References

[1] T.S. Cheng, J.A. Wehrmeyer, Pitz R.W., O. Jarrett, and G.B. Northam. Raman measurement of mixing and finite-rate chemistry in a supersonic hydrogen-air diffusion flame. *Combustion and Flame*, 99(1):157–173, 1994.

[2] W. Waidmann, U. Brummund, and J. Nuding. Experimental investigation of supersonic ramjet combustion (scramjet). In S. H. Chan, editor, *Transport Phenomena in Combustion*, volume 2, pages 1473–1484. Taylor and Francis, Washington, D.C., 1995.

[3] W. Waidmann, F. Alff, M. Bohm, U. Brummund, M. Clauss, and M. Oschwald. Supersonic combustion of hydrogen/air in a scramjet combustion chamber. *Space Technology*, 15(6):421–429, 1996.

[4] A. Cutler, P. M. Danehy, R. R. Springer, and D. P. DeLoach. Cars thermometry in a supersonic combustor for cfd code validation. 40th AIAA Aerospace Sciences Meeting and Exhibit. AIAA 2002-0743., January 2002. Reno, NV, USA.

[5] M.K. Smart, N.E. Hass, and A. Paull. Flight data analysis of the hyshot 2 scramjet flight experiment. *AIAA Journal*, 44(10):2366–2375, 2006.

[6] J. Steelant, R. Varvill, C. Walton, S. Defoort, K. Hannemann, and M. Marini. Achievements obtained for sustained hypersonic flight within the lapcat-ii project. 20th AIAA International Space Planes and Hypersonic Systems and Technologies Conference. AIAA 2015-3677, July 2015. Glasgow, Scotland.

[7] A. Vincent-Randonnier, Y. Moule, and M. Ferrier. Combustion of hydrogen in hot air flows within lapcat-ii dual mode ramjet combustor at onera-laerte facility - experimental and numerical investigation. 19th AIAA International Space Planes and Hypersonic Systems and Technologies Conference. AIAA 2014-2932, June 2014. Atlanta, GA, USA.

[8] M. Gamba and M. G. Mungal. Ignition, flame structure and near-wall burning in transverse hydrogen jets in supersonic crossflow. *Journal of Fluid Mechanics*, 780:226–273, 2015.

[9] A. Vincent-Randonnier, V. Sabelnikov, A. Ristori, N. Zettervall, and C. Fureby. An experimental and computational study of hydrogen–air combustion in the lapcat ii supersonic combustor. *Proceedings of the Combustion Institute*, 37(3):3703–3711, 2019.

[10] S. Balland and A. Vincent-Randonnier. Numerical study of hydrogen/air combustion with cedre code on laerte dual mode ramjet combustion experiment. 20th AIAA International Space Planes and Hypersonic Systems and Technologies Conference. AIAA 2015-3629, July 2015. Glasgow, Scotland.

[11] A. Refloch, B. Courbet, A. , Murrone, P. Villedieu, C. Laurent, P. Gilbank, J. Troyes, L. Tessé, G. Chaineray, J. B. Dargaud, E. Quémerais, and F. Vuillot. Cedre software. *AerospaceLab Journal*, Mar 2011.

[12] P. R. Spalart, S. Deck, M. L. Shur, K. D. Squires, M. Kh. Strelets, and A. Travin. A new version of detached-eddy simulation, resistant to ambiguous grid densities. *Theoretical and Computational Fluid Dynamics*, 20(3):181–195, 2006.

[13] M. Strelets. Detached eddy simulations of massively separated flows. 39th AIAA Aerospace Sciences Meeting and Exhibit, January 2001. Reno, NV, USA.

[14] F. Menter. Two-equation eddy-viscosity transport turbulence model for engineering applications. *AIAA Journal*, 32(8):1598–1605, Sep 1994.

[15] C-C. Fan, X. Xiao, J. R. Edwards, and H. A. Hassan. Hybrid large-eddy/reynolds-averaged navier–stokes simulations of shock-separated flows. *Journal of Spacecraft and Rockets*, 41(6):897–906, November-December 2004.

[16] J. Nikuradse. `stomungsgesetz in rahen rohren. *Forschg. Arb. Ing.-Wes*, 361, 1933.

[17] J. Nikuradse. Law of flows in rough pipes. Technical Report NACA TM 1292, National Advisory Committee for Aeronautics, 1937.

[18] P. M. Ligrani and R. J. Moffat. Structure of transitionally rough and fully rough turbulent boundary layers. *Journal of Fluid Mechanics*, 162:69–98, 1986.

[19] C. Grigson. Drag losses of new ships caused by hull finish. *Journal of Ship Research*, 36(2):182–196, 1992.

[20] B. Aupoix. Roughness corrections for the k-ω shear stress transport model: status and proposals. *Journal of Fluids Engineering*, 137(2):021202–1–021202–10, 2015.

[21] D. C. Wilcox. Reassessment of the scale-determining equation for advanced turbulence models. *AIAA Journal*, 26(11):1299–1310, 1988.

[22] D. C. Wilcox. Formulation of the k-ω turbulence model revisited. *AIAA Journal*, 46(11):2823–2838, 2008.

[23] A. Hellsten and S. Laine. Extension of k-ω shear-stress transport turbulence model for rough-wall flows. *AIAA Journal*, 36(9):1728–1729, 2008.

[24] T. Knopp, B. Eisfeld, and J. B. Calvo. A new extension for k-ω turbulence models to account for wall roughness. *International Journal of Heat and Fluid Flow*, 30(1):54–65, 2009.

[25] R. M. Latin and R. D. Bowersox. Flow properties of a supersonic turbulent boundary layer with wall roughness. *AIAA Journal*, 38(10):1804–1821, October 2000.

[26] C.J. Jachimowsky. An analytical study of hydrogen-air reaction mechanism with application to scramjet combustion. Technical Report TP-2791, NASA, February 1988.

[27] E.F. Toro, M. Spruce, and W. Speares. Restoration of the contact surface in the hll-riemann solver. *Shock Waves*, 4(1):25–34, 1994.

[28] B. Van Leer. Towards the ultimate conservative difference scheme. ii. monotonicity and conservation combined in a second-order scheme. *Journal of Computational Physics*, 14(4):361–370, 1974.

[29] B. Van Leer. Towards the ultimate conservative difference scheme. v. a second-order sequel to godunov's method. *Journal of Computational Physics*, 32(1):101–136, 1979.

[30] A. Techer, Y. Moule, G. Lehnasch, and A. Mura. Mixing of fuel jet in supersonic crossflow: estimation of subgrid scale scalar fluctuations. *AIAA Journal*, 56(2):465–481, February 2018.

[31] C. Yoo, R. Sankaran, and J. Chen. Three-dimensional direct simulation of a turbulent lifted hydrogen jet flame in heated coflow: flame stabilization and structure. *Journal of Fluid Mechanics*, 640:453–481, 2009.